



Extraordinary optical transmission in nano-bridged plasmonic arrays mimicking a stable weakly-connected percolation threshold

ESER METIN AKINOGLU,^{1,2,*}  LINGPENG LUO,^{1,3} TYLER DODGE,⁴ LIJING GUO,¹ GOEKALP ENGIN AKINOGLU,^{5,6} XIN WANG,^{1,3} LINLING SHUI,^{1,7} GUOFU ZHOU,^{1,3} MICHAEL J. NAUGHTON,⁴ KRZYSZTOF KEMPA,⁴ AND MICHAEL GIERSIG^{1,8}

¹International Academy of Optoelectronics at Zhaoqing, South China Normal University, Zhaoqing, 526238 Guangdong, China

²ARC Centre of Excellence in Exciton Science, School of Chemistry, University of Melbourne, Parkville, VIC, 3010, Australia

³Guangdong Provincial Key Laboratory of Optical Information Materials and Technology & Institute of Electronic Paper Displays, South China Academy of Advanced Optoelectronics, South China Normal University, 510006 Guangdong, China

⁴Boston College, Department of Physics, Chestnut Hill, MA 02467, USA

⁵Advanced Materials and BioEngineering Research Centre (AMBER), Trinity College Dublin, The University of Dublin, Dublin 2, Ireland

⁶The School of Chemistry, Trinity College Dublin, The University of Dublin, Dublin 2, Ireland

⁷School of Information Optoelectronic Science and Engineering, South China Normal University, 510006 Guangzhou, China

⁸Institute of Fundamental Technological Research, Polish Academy of Sciences, 02-106 Warsaw, Poland
[*e.a@fu-berlin.de](mailto:e.a@fu-berlin.de)

Abstract: Ultrasensitive sensors of various physical properties can be based on percolation systems, e.g., insulating media filled with nearly touching conducting particles. Such a system at its percolation threshold featuring the critical particle concentration, changes drastically its response (electrical conduction, light transmission, etc.) when subjected to an external stimulus. Due to the critical nature of this threshold, a given state at the threshold is typically very unstable. However, stability can be restored without significantly sacrificing the structure sensitivity by forming weak connections between the conducting particles. In this work, we employed nano-bridged nanosphere lithography to produce such a weakly connected percolation system. It consists of two coupled quasi-Babinet complementary arrays, one with weakly connected, and the other with disconnected metallic islands. We demonstrate via experiment and simulation that the physics of this plasmonic system is non-trivial, and leads to the extraordinary optical transmission at narrowly defined peaks sensitive to system parameters, with surface plasmons mediating this process. Thus, our system is a potential candidate for percolation effect based sensor applications. Promising detection schemes could be based on these effects.

© 2020 Optical Society of America under the terms of the [OSA Open Access Publishing Agreement](#)

1. Introduction

Ultrasensitive detectors of various physical properties often benefit from a highly nonlinear functional response of the employed detector structures. Such nonlinearities occur in systems with phase transitions, such as percolation structures [1], formed for example by randomly distributing conducting particles in a dielectric medium [2–4]. At the critical particle concentration, i.e. the percolation threshold, a phase transition occurs in the parameter space of such a structure, which radically changes its response (e.g. electrical conduction). It can be shown that this threshold represents the critical fixed point of the renormalization group transformation for this system,

implying an extreme nonlinear response [5]. Thus, this system, tuned by particle concentration to be very close to the threshold, can serve as a very sensitive detector of various physical properties such as temperature, pressure, presence of particles or molecules, optical radiation, etc. In fact, many detector systems indeed employ this strategy [6].

It was also demonstrated that the optical response can be drastically changed at a percolation threshold [7]. In one theoretical study, it was shown that a planar checkerboard structure, made by cutting square openings in a metallic film, is a self-Babinet, periodic structure at the percolation threshold [8]. Its optical, plasmonic response was shown to be highly nonlinear and chaotic. Similar optical percolation structures were experimentally realized by nanosphere lithography (NSL), which employs densely packed arrays of polystyrene spheres. Reducing the size of the spheres without changing their locations allows one to create lithographic templates, which form a percolation series of structures, ranging from arrays of isolated quasi-triangular particles, to arrays of circular holes [9]. The percolation threshold structure, in this case, is that with the circular holes just touching.

Sensor applications of percolation structures, however, remain very difficult to demonstrate. On one hand, their extreme nonlinearity is beneficial, as it can increase sensitivity. On the other hand, the critical nature of the threshold leads to notorious device instabilities; slight changes in design parameters drastically change the device characteristics. A solution to this problem was proposed and demonstrated in the context of the “impossible to measure” optical response of the self-Babinet checkerboard structure exactly at the percolation threshold [10]. This mathematically well-known response was finally measured successfully by changing the structure toward a slightly disconnected array of square islands, and then by making weak resistive links between the islands [10]. Briefly, the notion was to move away from the critical threshold point, toward the weakly connected state of the structure, just outside the threshold. Thus, the stability of the periodic percolation structures could be restored without significantly sacrificing the structure sensitivity, by forming weakly-connected island arrays.

Inspired by this discovery, we have developed an efficient, inexpensive method to fabricate such weakly connected island arrays. Shown schematically in Fig. 1, it is based on a modification of the aforementioned NSL technique. In its simplest version, NSL utilizes a substrate supporting a hexagonal closed-packed monolayer of polystyrene spheres (PS), as small as 200 nm in diameter, and then uses this array as a template (Fig. 1(a1)) for material (e.g. metal) deposition [11,12]. Various modifications of NSL have been developed. For example, PS can be annealed above the glass transition temperature, wherein the resulting PS particles become slightly flattened, narrowing the inter PS space. Using such structures as templates for metal deposition leads the deposited pattern to form quasi-triangles, shrinking in size with increasing annealing time [13,14]. Alternatively, the spheres can be reduced in size by plasma etching, while keeping their locations fixed [15,16], schematically shown in Fig. 1(a2). Using such structures as templates for deposition leads to a pattern of circular holes of controllable diameter in the deposited film (after removal of the spheres).

In recent work [17], we modified this process to induce nano-bridge formation between nearest neighbor spheres. This was achieved by spin-coating a styrene monomer solution on top of the NSL template prior to the plasma etching process. This nano-bridged NSL (NBSL), schematically shown in Fig. 1(b2) [17], was used here to develop the deposition templates. Such a template after metal deposition but without lift-off produces complementary pairs of structures as shown in Fig. 1(b3): an array of semi-spherical islands deposited on the PS, weakly interconnected via the nano-bridges, and an array of isolated metallic islands on the substrate, shadow-complementary to the island array. As shown below, these complementary structures have a measured plasmonic response in good agreement with finite difference time domain (FDTD) simulations, where the presence of the nanobridges strongly narrows the resonance peaks with high sensitivity to system parameters.

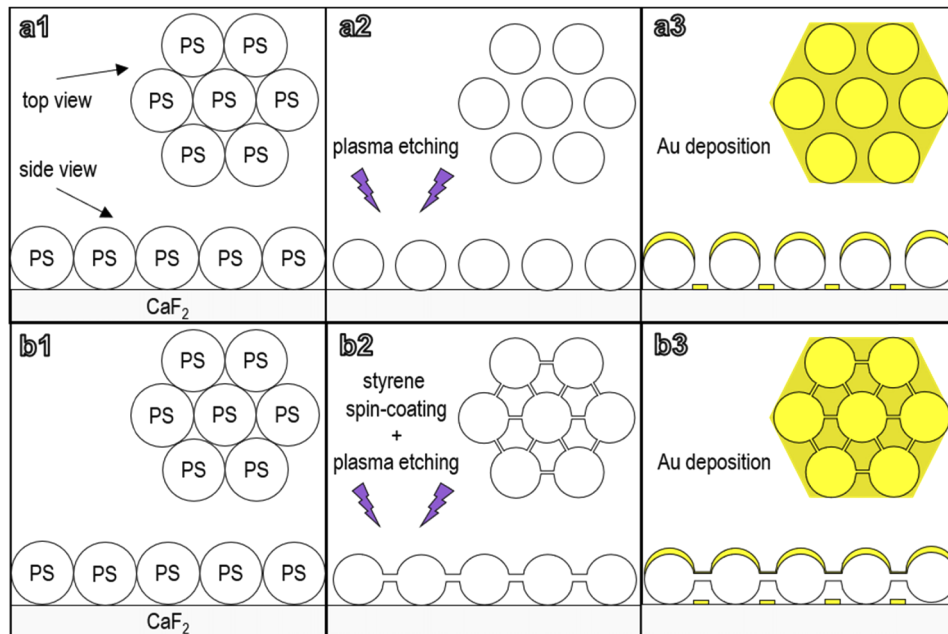


Fig. 1. Schematic illustrating the fabrication of disconnected (a) and nano-bridged (b) plasmonic arrays. In both cases a NSL template serves as the starting point (a1, b1). Plasma etching (a2) reduced the size of the individual PS spheres without displacing them. A pretreatment with a styrene solution induces the formation of nano-bridges (b2). Metallization with gold then yields disconnected (a3) and nano-bridged (b3) plasmonic arrays.

2. Methods

2.1. Sample fabrication and characterization

We used monodispersed PS (5% water suspensions, 784 nm diameter, and CV of 1.9% Wuhan Huge Biotechnology). A hexagonally closed-packed PS monolayer was self-assembled at a water-air interface and deposited on infrared-transparent CaF_2 substrates as described previously [18]. Subsequently, to obtain nano-bridge formation, 5 v% styrene in ethanol was spin-coated at 4,000 rpm for 30 sec, followed by oxygen plasma etch performed in a CY-P2L-B100 plasma cleaning system (Zhengzhou CY Scientific Instrument Co., Ltd) at 30 W power [17]. To obtain non-bridged arrays, the styrene treatment is omitted. However, for subtle etching, the nano-bridge formation occurs with and without the styrene treatment. The oxygen plasma etching of PS spheres depends on temperature, pressure and etchant to carrier gas ratio. Here, we used 5 SCCM flow of oxygen as the etchant gas and 2 SCCM Ar as the carrier gas. The total plasma pressure was 0.5 mbar at ambient temperature and the etching time was varied to control the final size of the PS particles. Plasma etching for 335 s, 300 s and 265 s was used to reduce the PS sphere size to 690 nm, 702 nm and 733 nm, respectively. Subsequently, 50 nm Au was deposited via electron beam evaporation. The morphologies of the samples were characterized by scanning electron microscopy (Zeiss, Sigma 500). Optical characterization was performed at room temperature using a Fourier-transform infrared (FTIR) spectrometer in transmission mode (Vertex 70v, Bruker Corporation). Note, that due to the spectrometer design, a large portion of the light scattered misses the detector [19], making it difficult to compare quantitatively with FDTD simulations, which include all scattering effects. We demonstrate below, that this scattered light can be accounted for phenomenologically, thus improving the agreement with simulations.

2.2. Simulations

Transmittance spectra were obtained using the finite difference time domain (FDTD) simulation method on the commercial Microwave Studio software package from CST [20]. Simulations were performed with appropriate periodic boundary conditions, that approximate a TEM wave of normal incidence on the plane of the PS spheres. Perfectly matched layers in the z direction hinder unwanted back reflections in the wave propagation direction. The CaF₂ substrate and PS spheres are modeled as dispersionless with refractive indexes $n = 1.4$ and 1.6 respectively, and the metal coating layer uses a Lorentz-Drude model for gold [21].

3. Results and discussion

The morphology of the nano-bridged and disconnected plasmonic arrays is shown in the SEM micrographs displayed in Fig. 2. The pitch of the periodic arrays is determined by the 784 nm diameter of the hexagonally closed-packed PS spheres prior to processing, with an error of 1.9% due to a small divergence from monodispersity. Nano-bridged plasmonic arrays with 690 nm and 702 nm, etched and metallized, sphere diameters are displayed in Fig. 2(a) and Fig. 2(b), respectively. Typically, the metallized caps of the individual PS spheres are connected to their nearest neighbors. The insets show magnified SEM micrographs that were imaged at 45° angle. Here, the details of the nano-bridges are evident: the nano-bridges form seamless metallized connections between the gold-coated PS sphere caps. Simultaneously, Au is found on the CaF₂ substrate between the individual PS spheres and nano-bridges, a consequence of their shadowing during metallization. Equivalent structures without the nano-bridges but with the same dimensions, *i.e.* disconnected plasmonic arrays, are shown in Fig. 2(c) and Fig. 2(d), respectively. In this case, the Au cap at the apex of each individual PS sphere is disconnected from all its nearest neighbors and the shadow-deposited gold on the CaF₂ substrate forms a periodically perforated gold thin film. Consequently, these structures consist of two plasmon active, periodic, metallic slabs that are vertically separated by a submicron distance.

First, we consider the nano-bridged case. Here, the bottom array (on the substrate) consists of the shadow-defined pattern of the spheres and nano-bridges, and yields disconnected islands. As this array is disconnected, its electrical resistance diverges. The top array is composed of semi-spherical islands (the caps of the deposited material on each PS), with each island weakly connected to its nearest neighbor along the coated nano-bridges. The resistance of this top array is finite, and limited by the size and material properties of the links. Thus, the in-plane resistance of the two simultaneously measured arrays is determined by the top layer, and the system acts as a weakly connected array of islands near the percolation threshold, which typically results in a high sensitive to parameter changes. In the absence of nano-bridges, the bottom slab is an array of holes in a deposited film and thus conductive. Consequently, it is little affected by parameter changes. The upper slab consists of an array of disconnected gold caps, thus having diverging in-plane resistance. In either case, the arrays form proximity-coupled, shadow-complementary quasi-Babinet structures.

Such vertically coupled Babinet complementary plasmonic arrays have been exploited for visible light applications such as plasmonic pixels and surface enhanced Raman spectroscopy studies [22–27]. Furthermore, the visible optical response of disconnected plasmonic arrays based on plasma-etched PS spheres metallized with gold were studied, and revealed that it is possible to tune the wavelength and the locations of the enhanced plasmonic fields within the nanostructure [28]. A simpler structure was studied recently using FDTD simulations and showed a remarkable optical response in the infrared [29]. It was shown that this structure exhibits extraordinary transmission (EOT) [24] at a plasmon resonance and that, due to the underlying Babinet physics of these coupled arrays, the spectral width of the plasmonic resonances was reduced, and the higher harmonics suppressed.

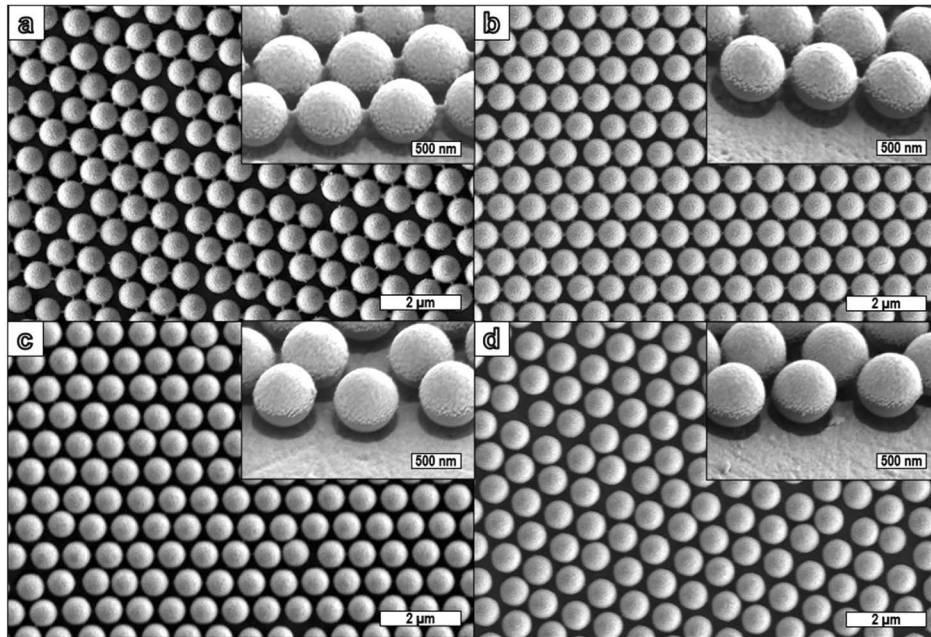


Fig. 2. SEM images of nano-bridged and disconnected plasmonic arrays. The pitch of the arrays is 784 nm. (a) nano-bridges with 690 nm diameter spheres, (b) nano-bridges with 702 nm diameter spheres, (c) disconnected with 690 nm diameter spheres, (d) disconnected with 702 nm diameter spheres. The insets show details of the nano-bridges or voids between the spheres from a 45° perspective.

The spectral response of our disconnected and nano-bridged structures is also controlled by the Babinet plasmonics, which as will be shown below leads to the surprisingly large long wavelength transmittance, even though these are highly metalized structures with $\sim 100\%$ projected metal coverage. The basic physics can be identified even with simple metamaterial arguments. Consider the simplest model of the Babinet pair of layers, as sketched in the top panel of Fig. 3(a), with an array of metallic islands (brown rectangles) in the upper layer, and the corresponding aligned complementary array of holes just below. The in-plane component of the electric field of the incoming wave, with wavelengths long in comparison to the geometrical structure details, induces (at an instant of time) a displacement of electron gas in the metallic structures, which results in the surface charge build-up (red and blue colors). Note the reversed charge polarization on different layers. Each layer can be viewed as an array of antennas driven by an initial wave, that re-radiate electromagnetic waves. In the absence of the second layer, the re-radiated wave by the first array would tend to cancel the initial wave moving forward at large distances, as all metals do. This would lead to vanishing transmission, and large back reflection. However, in the presence of the second layer, the wave reradiated by the second array cancels-out the action of the first layer antenna array, and thus the initial wave can easily penetrate the structure largely unperturbed. The lower panel in Fig. 3(a) shows a color map of the electric field magnitudes in our structure, and confirms the charging scheme implied in the upper panel of Fig. 3(a).

The above analysis, which only roughly explains the high transparency of the highly metalized Babinet bi-layer, can be made more rigorous by employing the effective medium picture of the Babinet arrays [8]. The effective susceptibility of an island array layer at frequency ω can be written as $\chi(\omega) = \bar{\omega}^2 \frac{A}{B}$, where $A = \prod_n (\omega_{0n}^2 - \omega^2)$, $B = \prod_n (\omega_m^2 - \omega^2)$, and $\bar{\omega}$ is a constant. When negligible metallic losses can be assumed, $\chi(\omega)$ is real, and is sketched in the

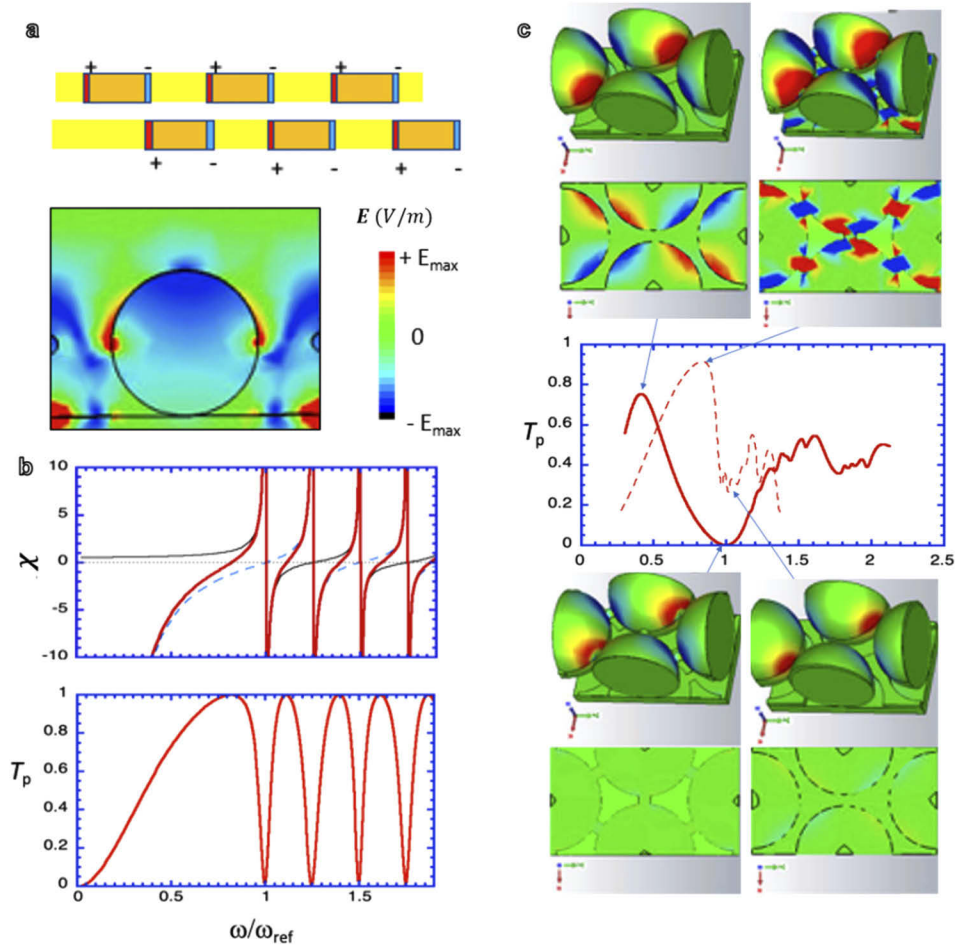


Fig. 3. Model of the Babinet pair of layers (a, top panel). A color map of the electric field magnitudes in our bridged structure at maximum of transmission (a, bottom panel). The effective medium picture of the Babinet arrays: (b, top panel) shows the electronic susceptibilities $\chi(\omega)$ (thin-solid line), $\chi_c(\omega)$ (thin-dashed line) and $\chi_p(\omega)$ (thick-solid line); (b, bottom panel) shows the simulated T_p vs ω . FDTD for complementary Babinet pairs following Eq. (1). (c) shows T_p for the bridged (thin-dashed line) and disconnected (thick-solid line) Babinet pairs. Both curves are for spheres of diameter $d = 702$ nm. The 4 insets show the electric field simulations of the two complementary slabs at 4 spectral locations on the main plot, identified by the arrows. The color code of the electric field is the same as in (a).

top panel of Fig. 3(b) as a thin solid line. The corresponding complementary array of holes has corresponding susceptibility $\chi_c(\omega) = -\left(\frac{\omega_d}{\omega}\right)^2 \frac{B}{A}$ (where $\omega_d = 2c/d'$, with d' the film thickness) displayed as a dashed line in Fig. 3(b). The effective susceptibility of the Babinet pair is simply $\chi_p(\omega) = \chi(\omega) + \chi_c(\omega)$, and this is displayed as a thick solid line in the top panel of Fig. 3(b). Transmittance through this pair is then given by

$$T_p = 1 / \left[1 + \left(\frac{\omega}{\omega_d} \right)^2 \chi_p(\omega)^2 \right] \quad (1)$$

A sketch of T_p is shown in the bottom panel of Fig. 3(b). Since $\left(\frac{\omega}{\omega_d}\right)^2 = \pi^2\left(\frac{\bar{d}}{\lambda}\right)^2 \ll 1$ (\bar{d} is the combined layer thickness), large maxima of $T_p \approx 1$ can occur at conditions leading to vanishing, or simply small (of order 1) values of $|\chi_p(\omega)|$. The existence of a surface plasmon requires $|\chi_p(\omega)| = 2$, and thus satisfies this condition. This confirms, that like in the conventional EOT, the surface plasmons play a key role in boosting transmittance in our case.

The basic structure of the transmittance sketched in the bottom panel of Fig. 3(b), consisting of multiple transmittance maxima, valid for both bridged and disconnected Babinet pairs is reproduced by our FDTD simulations, displayed in the main plot of Fig. 3(c). Moreover, the electric field simulations of the top and bottom layers (shown in 3 color field distribution panels around the main plot), fully confirm the main physics discussed above and sketched in Fig. 3(a): the minima of T_p occur when only the top layer is active (see 2 bottom color panels), and the T_p maxima require the field canceling activity of both layers (see 2 top color panels).

Figure 4 shows experimental T_p spectra (versus vacuum wavelength of the incoming wave) for our disconnected Fig. 4(a) and bridged Fig. 4(b) structures. The corresponding FDTD simulated results are shown in Fig. 4, for disconnected Fig. 4(c) and bridged Fig. 4(d) structures. Note, that the two plots in Fig. 3 are identical to those plotted in Fig. 4(c) and Fig. 4(d), except for the change of the horizontal axis from eV into wavelength.

Even though there is some similarity between the experimental and simulated results regarding peak width and the main peak locations, there is also a major discrepancy: the simulated transmittance seems much stronger than the experimental one. This is a measurement artefact.

While simulations collect all transmitted radiation, the FTIR setup misses the stray scattered light. However, this can be corrected by writing

$$T_p = T_{exp} \sigma \quad (2)$$

where σ is the relative scattering cross section. The simplest model formula, which accounts for the dominant Rayleigh and Mie scattering mechanisms, and which agrees with computations in Ref. [27] is

$$\sigma = \frac{A}{1 + B\lambda^4} \quad (3)$$

where A and B are parameters of this phenomenological model. For sufficiently large B (or sufficiently large λ) this formula reduces to $\sigma = A/B\lambda^4$, i.e. the Rayleigh scattering dominates, and strongly depletes the forward transmitted light of short wavelength components (the blue-sky effect). In the other limit of large scatterers one expects the Mie scattering to dominate [30], which is characterized by large forward directionality of the scattered light (larger T_p), and weak dependency on λ . In our model, this occurs for sufficiently small B (or sufficiently small λ), which leads to $\sigma \rightarrow A$, i.e. a simple one parameter scaling. Using Eq. (1), with σ given by Eq. (2) and T_{exp} from Fig. 4(a) and Fig. 4(b), we obtain Fig. 4(e) and Fig. 4(f), respectively. Optimizing an agreement with simulations required us to employ our model in the Mie limit when correcting the structures without nanobridges ($B = 0$), and in the mixed Rayleigh-Mie limit for the structures with nanobridges present approximated with ($B = 0.001 \text{ um}^{-4}$). The values for A are derived from a least-squares fit. This is fully consistent with the scattering theory, since the Rayleigh scattering is strongly favored when very small (as compared to λ) scatterers (nanobridges) are present. The corrected experimental curves, shown in Fig. 4(e) and Fig. 4(f), agree with our simulations much better. Field animations in [Visualization 1](#), [Visualization 2](#), [Visualization 3](#) (Supplementary Materials online) demonstrate simulated stray scattering induced by modeled boundaries of our structure. In contrast to the simple phenomenological approach used above, microscopic simulations of the stray scattering are sample-size dependent, and require models with broken in-plane periodicity, or defects, which are very computationally expensive.

The observed high sensitivity of the transmission through our bridged structure at fixed frequency, by taking advantage of the very large slope of T_p (e.g. at $\lambda = 4 \text{ um}$) would be very

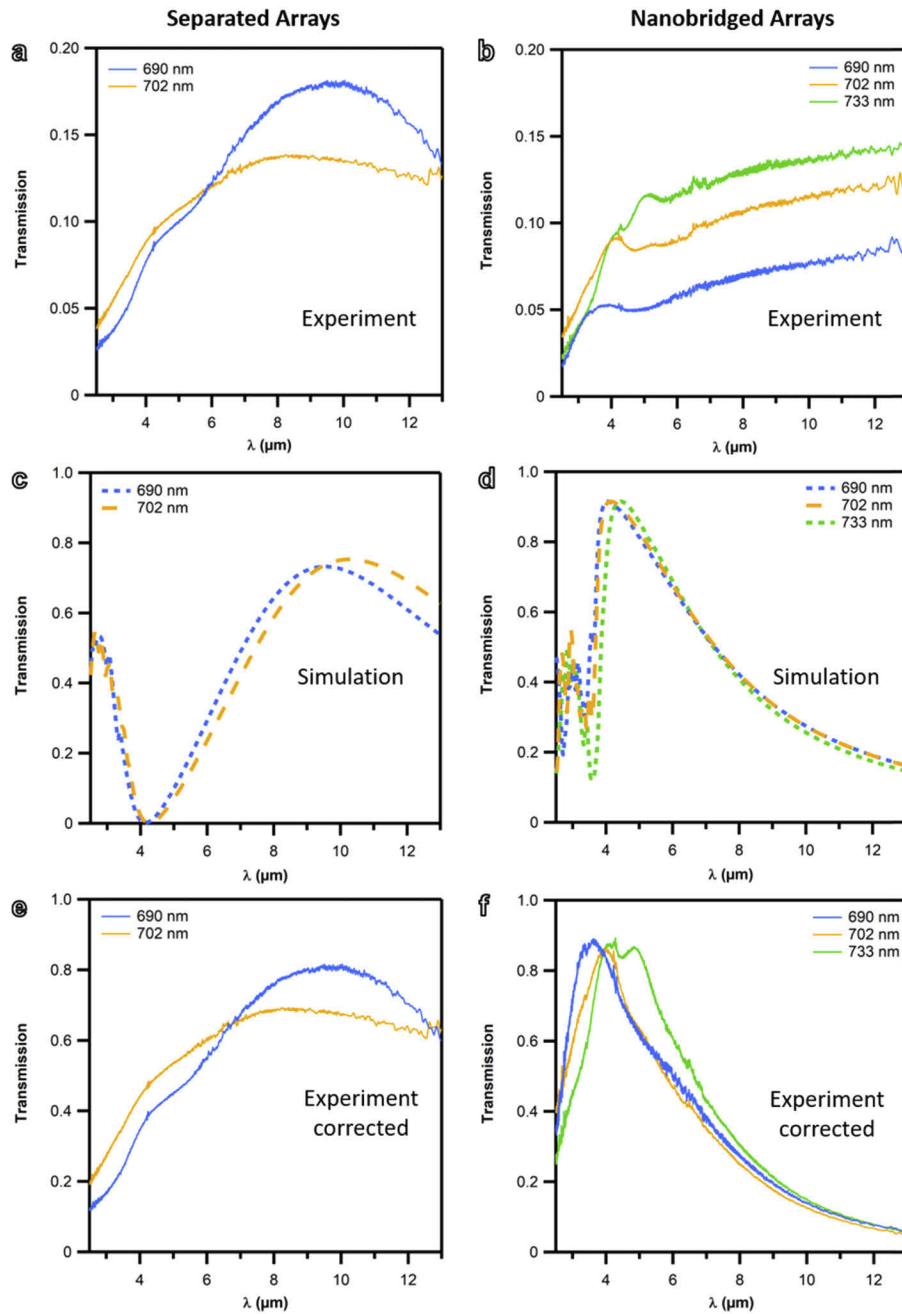


Fig. 4. Transmittance spectra for the coupled quasi-complementary plasmonic arrays in the infra-red wavelengths range. Experimental results for (a) separated and (b) nanobridged arrays, parametrized with the sphere diameters. Corresponding simulated results are shown in panels (c) and (d) respectively. (e) and (f) are the corresponding experimental results, corrected for scattering using Eq. (1) and the phenomenological model Eq. (2). Model parameters used to obtain (e) are: $B = 0$, and $A = 5$ ($d = 702$ nm), $A = 4.5$ ($d = 690$ nm). Model parameters used to obtain (f) are: $B = 0.001 \mu\text{m}^{-4}$, and $A = 0.0013$ ($d = 733$ nm), $A = 0.0012$ ($d = 702$ nm), and $A = 0.002$ ($d = 690$ nm). Vibrational modes of water vapor and CO_2 are observed that are caused by slight fluctuations of the atmospheric conditions. The CO_2 peaks are positioned at $4.27 \mu\text{m}$ (2343 cm^{-1}) and $4.38 \mu\text{m}$ (2283 cm^{-1}) and multiple peaks of water vapor are located around $6.6 \mu\text{m}$ (1515 cm^{-1}).

easy to measure, and could lead to inexpensive detectors. Finally, note that the in-plane resistance of our structure should in principle be also sensitive to similar, slight parameter modifications, making sensor applications even more facile. Such possibilities will be investigated elsewhere.

4. Conclusions

In this work, we developed a method to inexpensively fabricate a new plasmonic structure which is stable at its percolation threshold, with potential for sensor applications. Our procedure is a modified, conventional nanosphere lithography, in which the polystyrene spheres in the array are connected via nanobridges. By vertical metal deposition of metal (without a lift-off), one generates coupled, shadow-complementary quasi-Babinet metallic arrays near the percolation threshold, with nanobridges playing an important role of smoothing-out the criticality. We show via experiment and simulation that the main plasmonic effect is the EOT highly sensitive to variations of the system parameters. This effect can be used as a basis for high sensitivity, inexpensive sensors.

Funding

Guangdong Innovative and Entrepreneurial Team Program (2016ZT06C517); Australian Research Council (CE170100026); Science and Technology Program of Guangzhou (2019050001); Guangdong Special Fund Project of Science and Technology Application (2017B020240002); Alexander von Humboldt-Stiftung (Feodor Lynen Research Fellowship).

Acknowledgments

E.M.A. thanks the Alexander von Humboldt Foundation for its support with a Feodor Lynen Research Fellowship.

Disclosures

The authors declare that there are no conflicts of interest related to this article.

References

1. B. J. Last and D. J. Thouless, "Percolation Theory and Electrical Conductivity," *Phys. Rev. Lett.* **27**(25), 1719–1721 (1971).
2. M. Gaio, M. Castro-Lopez, J. Renger, N. van Hulst, and R. Sapienza, "Percolating plasmonic networks for light emission control," *Faraday Discuss.* **178**, 237–252 (2015).
3. H. Chen, F. Wang, K. Li, K. C. Woo, J. Wang, Q. Li, L.-D. Sun, X. Zhang, H.-Q. Lin, and C.-H. Yan, "Plasmonic percolation: plasmon-manifested dielectric-to-metal transition," *ACS Nano* **6**(8), 7162–7171 (2012).
4. W. Xia and F. M. Thorpe, "Percolation properties of random ellipses," *Phys. Rev. A* **38**(5), 2650–2656 (1988).
5. J. Cardy, *Scaling and Renormalization in Statistical Physics* (Cambridge University, 1996).
6. R.-F. Wu, W. Pan, S.-L. Shi, and R.-B. Han, "Critical behaviors of the conductivity and dielectric constant of Ti₃SiC₂/Al₂O₃ hybrids," *J. Appl. Phys.* **102**(5), 056104 (2007).
7. D. J. Bergman and Y. Imry, "Critical Behavior of the Complex Dielectric Constant near the Percolation Threshold of a Heterogeneous Material," *Phys. Rev. Lett.* **39**(19), 1222–1225 (1977).
8. K. Kempa, "Percolation effects in the checkerboard Babinet series of metamaterial structures," *Phys. Status Solidi RRL* **4**(8-9), 218–220 (2010).
9. E. M. Akinoglu, T. Sun, J. Gao, M. Giersig, Z. Ren, and K. Kempa, "Evidence for critical scaling of plasmonic modes at the percolation threshold in metallic nanostructures," *Appl. Phys. Lett.* **103**(17), 171106 (2013).
10. Y. Urade, Y. Nakata, T. Nakanishi, and M. Kitano, "Frequency-Independent Response of Self-Complementary Checkerboard Screens," *Phys. Rev. Lett.* **114**(23), 237401 (2015).
11. C. L. Haynes and R. P. van Duyne, "Nanosphere Lithography. A Versatile Nanofabrication Tool for Studies of Size-Dependent Nanoparticle Optics," *J. Phys. Chem. B* **105**(24), 5599–5611 (2001).
12. J. C. Hulst, "Nanosphere lithography. A materials general fabrication process for periodic particle array surfaces," *J. Vac. Sci. Technol., A* **13**(3), 1553–1558 (1995).
13. B. J. Y. Tan, C. H. Sow, T. S. Koh, K. C. Chin, A. T. S. Wee, and C. K. Ong, "Fabrication of Size-Tunable Gold Nanoparticles Array with Nanosphere Lithography, Reactive Ion Etching, and Thermal Annealing," *J. Phys. Chem. B* **109**(22), 11100–11109 (2005).

14. A. Kosiorek, W. Kandulski, H. Glaczynska, and M. Giersig, "Fabrication of nanoscale rings, dots, and rods by combining shadow nanosphere lithography and annealed polystyrene nanosphere masks," *Small* **1**(4), 439–444 (2005).
15. J. A. Yabagi, M. I. Kimpa, M. N. Muhammad, N. Nayan, Z. Embong, and M. A. Agam, "Nanofabrication Process by Reactive Ion Etching of Polystyrene Nanosphere on Silicon Surface," *Journal of Science and Technology* **9**, 145–153 (2017).
16. E. M. Akinoglu, A. J. Morfa, and M. Giersig, "Understanding anisotropic plasma etching of two-dimensional polystyrene opals for advanced materials fabrication," *Langmuir* **30**(41), 12354–12361 (2014).
17. L. Luo, E. M. Akinoglu, L. Wu, T. Dodge, X. Wang, G. Zhou, M. J. Naughton, K. Kempa, and M. Giersig, "Nano-bridged nanosphere lithography," *Nanotechnology* **31**(24), 245302 (2020).
18. E. M. Akinoglu, A. J. Morfa, and M. Giersig, "Nanosphere lithography – exploiting self-assembly on the nanoscale for sophisticated nanostructure fabrication," *Turk. J. Phys.* **38**, 563–572 (2014).
19. P. Bassan, A. Sachdeva, A. Kohler, C. Hughes, A. Henderson, J. Boyle, J. H. Shanks, M. Brown, N. W. Clarke, and P. Gardner, "FTIR microscopy of biological cells and tissue: data analysis using resonant Mie scattering (RMieS) EMS algorithm," *Analyst* **137**(6), 1370–1377 (2012).
20. CST Microwave Studio, Computer Simulation Technology AG, <http://www.cst.com/products/cstmws>.
21. E. J. Zeman and G. C. Schatz, "An accurate electromagnetic theory study of surface enhancement factors for silver, gold, copper, lithium, sodium, aluminum, gallium, indium, zinc, and cadmium," *J. Phys. Chem.* **91**(3), 634–643 (1987).
22. W.-D. Li, F. Ding, J. Hu, and S. Y. Chou, "Three-dimensional cavity nanoantenna coupled plasmonic nanodots for ultrahigh and uniform surface-enhanced Raman scattering over large area," *Opt. Express* **19**(5), 3925–3936 (2011).
23. Y. Gu, L. Zhang, J. K. W. Yang, S. P. Yeo, and C.-W. Qiu, "Color generation via subwavelength plasmonic nanostructures," *Nanoscale* **7**(15), 6409–6419 (2015).
24. C. Williams, G. Rughoobur, A. J. Flewitt, and T. D. Wilkinson, "Nanostructured plasmonic metapixels," *Sci. Rep.* **7**(1), 7745 (2017).
25. R. Mudachathi and T. Tanaka, "Up Scalable Full Colour Plasmonic Pixels with Controllable Hue, Brightness and Saturation," *Sci. Rep.* **7**(1), 1199 (2017).
26. J. D. Caldwell, O. Glembocki, F. J. Bezares, N. D. Bassim, R. W. Rendell, M. Feygelson, M. Ukaegbu, R. Kasica, L. Shirey, and C. Hosten, "Plasmonic nanopillar arrays for large-area, high-enhancement surface-enhanced Raman scattering sensors," *ACS Nano* **5**(5), 4046–4055 (2011).
27. G. E. Akinoglu, S. H. Mir, R. Gatensby, G. Rydzek, and P. Mokarian-Tabari, "Block Copolymer Derived Vertically Coupled Plasmonic Arrays for Surface-Enhanced Raman Spectroscopy," *ACS Appl. Mater. Interfaces* **12**(20), 23410–23416 (2020).
28. C. A. Tira, I. Ly, R. A. L. Vallee, S. Astilean, and C. Farcau, "Shaping light spectra and field profiles in metal-coated monolayers of etched microspheres," *Opt. Mater. Express* **7**(8), 2847–2859 (2017).
29. G. E. Akinoglu, E. M. Akinoglu, K. Kempa, and M. Giersig, "Plasmon resonances in coupled Babinet complementary arrays in the mid-infrared range," *Opt. Express* **27**(16), 22939–22950 (2019).
30. A. J. Cox, A. J. DeWeerd, and J. Linden, "An experiment to measure Mie and Rayleigh total scattering cross sections," *Am. J. Phys.* **70**(6), 620–625 (2002).

